

Oscillatory shear-induced bcc-fcc martensitic transformation in a colloidal suspension with long-range repulsive interactions

Cite as: J. Chem. Phys. **154**, 164903 (2021); <https://doi.org/10.1063/5.0045537>

Submitted: 27 January 2021 • Accepted: 02 April 2021 • Published Online: 23 April 2021

 Giulia Fiorucci and  Marjolein Dijkstra

COLLECTIONS

Paper published as part of the special topic on [Special Collection in Honor of Women in Chemical Physics and Physical Chemistry](#)



View Online



Export Citation



CrossMark

ARTICLES YOU MAY BE INTERESTED IN

[Characterization of MIPS in a suspension of repulsive active Brownian particles through dynamical features](#)

The Journal of Chemical Physics **154**, 164901 (2021); <https://doi.org/10.1063/5.0040141>

[Point defects in crystals of charged colloids](#)

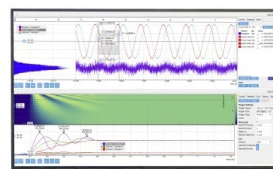
The Journal of Chemical Physics **154**, 164905 (2021); <https://doi.org/10.1063/5.0047034>

[Effects of interfaces on structure and dynamics of water droplets on a graphene surface: A molecular dynamics study](#)

The Journal of Chemical Physics **154**, 164704 (2021); <https://doi.org/10.1063/5.0046817>

Challenge us.

What are your needs for
periodic signal detection?



Zurich
Instruments

Oscillatory shear-induced bcc-fcc martensitic transformation in a colloidal suspension with long-range repulsive interactions

Cite as: J. Chem. Phys. 154, 164903 (2021); doi: 10.1063/5.0045537

Submitted: 27 January 2021 • Accepted: 2 April 2021 •

Published Online: 23 April 2021



View Online



Export Citation



CrossMark

Giulia Fiorucci  and Marjolein Dijkstra^{a)} 

AFFILIATIONS

Soft Condensed Matter, Debye Institute for Nanomaterials Science, Department of Physics, Utrecht University, Princetonplein 1, 3584 CC Utrecht, The Netherlands

Note: This paper is part of the JCP Special Collection in Honor of Women in Chemical Physics and Physical Chemistry.

^{a)} Author to whom correspondence should be addressed: m.dijkstra@uu.nl

ABSTRACT

We perform non-equilibrium Brownian dynamics simulations to investigate the out-of-equilibrium phase behavior of a suspension of charged colloids under external oscillatory shear. We independently vary the frequency f and the maximum strain amplitude γ_{\max} of the oscillations and map out an out-of-equilibrium phase diagram in the f - γ_{\max} plane. Similar to what has been observed in earlier studies on colloidal hard spheres, we find the formation of a twinned face-centered-cubic phase in a specific range of γ_{\max} , which displays a martensitic transition to a body-centered-cubic crystal within half of the oscillation cycle. We provide a comprehensive analysis of these structures and show how the system transforms from one to the other. We also report evidence of a sliding layer phase and a string phase.

Published under license by AIP Publishing. <https://doi.org/10.1063/5.0045537>

I. INTRODUCTION

Colloidal science has invested much research on understanding the intricate coupling between the structure of matter and the physical properties it exhibits. It is well known that the spatial organization of matter on the microscopic scale determines the properties of the system on the macroscopic scale. In reverse, it is possible to fabricate a system that manifests the desired physical properties by driving the formation of specific microstructures. The significance of this branch of research is due to the numerous industrial applications of colloidal suspensions in emerging technologies. For instance, specific colloidal structures reveal intriguing optical properties such as photonic crystals, where the material exhibits a photonic bandgap that prevents the propagation of light along specific directions.^{1,2} Other unexpected discoveries are made in rheology, which studies the mechanical properties of fluids under shear stress. In non-Newtonian fluids, the application of steady or oscillatory shear is responsible for the aggregation of colloidal suspensions on a local level, determining a change in the visco-elastic properties of the system. These phenomena are known as shear thinning, shear thickening, and shear banding.³⁻⁷

Although major steps toward the comprehension of soft condensed matter have been performed, having control over the self-assembly process is still a major challenge. The self-assembly process may be assisted by means of external fields, such as electric or magnetic fields, laser-optical fields, and shearing⁸ or flow fields in microfluidic devices.^{9,10}

During the past three decades, a branch of research has focused on the application of steady and oscillatory shear to suspensions of hard spheres and charged particles.¹¹ Surprisingly, it has been discovered that steady and oscillatory shear induces crystal formation in a fluid of hard spheres, and the shear-induced crystal melts back upon cessation of the shear.^{12,13} This out-of-equilibrium shear-induced crystallization is the result of a delicate balance of direct interparticle interactions, Brownian motion, shear-flow induced dynamics, and hydrodynamic interactions.

Understanding shear-induced ordering of colloidal fluids is technologically relevant for, e.g., ink printing, paints, or coatings. Additionally, the possibility to switch between different states upon application of an external field is promising for, e.g., electronic ink displays, in which one can switch between an ordered state displaying color by interference to a disordered state without any color.

In a steady and oscillating shear flow, the strain amplitude is one of the key parameters that drives the self-assembly process. This parameter sets the distance of flow-induced interactions between the particles. By varying the strain amplitude, a rich out-of-equilibrium phase diagram displaying layering,¹⁴ string formations,¹⁵ and 3D crystal-like ordering^{13,16} has been observed in experimental and numerical studies of hard and nearly hard spheres. For low values of the strain amplitude, the system forms the twinned face-centred-cubic (fcc) structures.^{12,13,16,17} For higher strain amplitudes, the crystal ordering is affected by the collisions among particles, which become more frequent. The hexagonal order on the velocity–vorticity plane is preserved, but the planes along the gradient direction show random stacking. This different phase is known as the sliding layer phase and was observed by several experimental groups.^{13,16,17} A comprehensive investigation of the out-of-equilibrium phase behavior of hard-sphere-like colloidal suspensions is reported in Ref. 16, where the authors provide an analysis of different ordered structures encountered by systematically varying the strain amplitude and the oscillation frequency. This combined experimental and simulation study performed on hard-sphere particles demonstrates that oscillatory shear is a valuable method to generate non-equilibrium ordered structures out of a disordered fluid phase.

In analogy, some work has been performed on charged colloidal particles. Yan *et al.* performed a light scattering study on weakly repulsive charged colloids under oscillatory shear.¹⁸ They distinguished two ordered structures by varying the strain amplitude: the twinned fcc phase for low strain and the sliding layer phase at high strain. These results are in agreement with the earlier mentioned studies on hard spheres, which is to be expected since the Debye screening length is just about 6% of the particle diameter. In addition, it was shown that the application of steady shear and confining walls also induces a sliding layer phase in a charged colloidal suspension^{19–21} and a transformation from a bcc-dominated to a fcc-dominated crystal in a suspension of ultrasoft star polymers.²² Furthermore, Xue and Grest investigated the behavior of repulsive particles characterized by a longer range of interaction.²³ They implemented Non-Equilibrium Brownian Dynamics (NEBD) simulations and found shear-induced string ordering in a system at temperatures slightly below the melting point. The strings are aligned along the velocity axis, forming hexagonal packing in the vorticity–gradient plane. Beyond this result, they did not find any evidence of 3D ordered structures. However, they investigated only low values of the Péclet number (Pe), where the Brownian forces might still be sufficiently strong compared to the convective drag induced by the shearing. To the best of our knowledge, a comprehensive study on the effect of oscillatory shear on an equilibrium fluid of long-range repulsive particles just below the fluid-bcc freezing transition is still missing in the literature.

Hence, we investigate in this paper the effect of oscillatory shear on a colloidal fluid of long-range repulsive particles using NEBD simulations without including hydrodynamic interactions among the colloids. We remark that the opposite phenomenon of shear-melting colloidal crystals has already been investigated in 1991.²⁴ In the case of a hard-sphere fluid at a density just below the freezing transition to an fcc phase, a twinned fcc phase was observed upon application of oscillatory shear.^{12,16} Here, we investigate whether such a twinned fcc phase is also induced by

oscillatory shear in a fluid of long-ranged repulsive spheres at a density close to the fluid-bcc freezing transition. Rather remarkably, we, indeed, observe such an oscillatory shear-induced twinned fcc phase in a long-range repulsive system, displaying a martensitic transition to a body-centered-cubic (bcc) crystal. The martensitic phase transition has been studied in various colloidal systems by using electric fields,^{25,26} tuning the volume fractions,^{27–29} particle shapes,^{30,31} depletants,³² and DNA linkers,^{33,34} and various transformation pathways have been reported. In this paper, we analyze in detail the transformation mechanism of the martensitic transition of the shear-induced twinned fcc phase. Finally, we map out the out-of-equilibrium phase behavior as a function of maximum strain amplitude and frequency of oscillation. The resulting out-of-equilibrium phase diagram exhibits a fluid phase, a string phase, a sliding layer phase, and a twinned fcc phase. We compare our observations with the oscillatory shear-induced phase behavior of a fluid of hard-sphere colloids near the fluid-fcc phase transition.

This paper is organized as follows. In Sec. II, we describe our model and present the methods that we use to simulate the system and to analyze the results. The results are presented and discussed in Sec. III, and we make some concluding remarks in Sec. IV.

II. MODEL AND METHODS

A. The model system

We consider a system of charge-stabilized colloidal particles in the presence of an oscillating shear flow. We model the interaction between two hard-sphere colloids with a diameter σ through a screened Coulomb (Yukawa) potential,

$$\beta U(r) = \begin{cases} \beta \epsilon \frac{\exp[-\kappa \sigma (r/\sigma - 1)]}{r/\sigma} & r > \sigma \\ \infty & r \leq \sigma, \end{cases} \quad (1)$$

where r denotes the interparticle distance, $\beta \epsilon$ is the repulsion energy at contact distance $r = \sigma$, and $\kappa \sigma$ is the inverse Debye screening length. We use $1/\beta = k_B T$ as our unit of energy with k_B the Boltzmann constant and T the temperature of the system. The phase diagrams of these hard-core Yukawa systems have been determined using Monte Carlo simulations as a function of inverse screening length $\kappa \sigma$ and packing fraction $\phi = \pi \sigma^3 N/6V$, and display a stable fluid phase, an fcc phase, and a bcc phase at sufficiently low screening.³⁵ In this work, we simulate a fluid phase at a volume fraction of $\phi = 0.085$, $\beta \epsilon = 80$, and $\kappa \sigma = 2$, which is just below the fluid-bcc freezing packing fraction $\phi_f = 0.092$. For a system with such a dilute density $\rho = N/V$ and high repulsion energy $\beta \epsilon$, the averaged interparticle distance $\rho^{-1/3} = 1.83\sigma$ is always larger than σ , and hence, this system is well-described by a point-Yukawa system, as demonstrated in Ref. 35 to which we refer the interested reader for more details on this mapping. Consequently, we simplify our simulation method by implementing only the Yukawa repulsion term of Eq. (1), whereas we neglect the hard-core repulsion term and perform a post-clearance verification that particles do not approach each other closer than σ by analyzing the radial distribution function of the system.

As illustrated in Fig. 1, we confine the system in the z direction with two soft repulsive planar walls, located at $z = 0$ and $z = h$, in order to match the experimental setup of a parallel plate shear cell.¹⁶ Hence, a particle positioned at height z interacts with the walls according to

$$\beta U_w(z) = \begin{cases} \beta \epsilon_w \left(\frac{\sigma}{z}\right)^6 & \text{for } z < \sigma/2 \\ \beta \epsilon_w \left(\frac{\sigma}{h-z}\right)^6 & \text{for } z > h - \sigma/2 \\ 0 & \text{otherwise,} \end{cases} \quad (2)$$

where $\beta \epsilon_w = 2.5$ is the wall–particle repulsion energy. Note that we use periodic boundary conditions in the x - and y -direction. The phase behavior of charged colloids confined between two planar soft walls at small plate separations has been studied both experimentally and in simulations,³⁶ showing a sequence of multilayered structures with rhombic, triangular, quadratic, and rectangular symmetry upon increasing plate separation. Here, we consider, however, a fluid of charged colloids at a much larger plate separation, where only pronounced layering of the fluid is induced in the vicinity of the walls.

We perform simulations by implementing the Non-Equilibrium Brownian Dynamics (NEBD) technique. This method enables us to reproduce the colloidal dynamics in the presence of an external oscillatory shear. Note that this technique does not include hydrodynamic interactions among the colloids. We integrate the position \mathbf{r}_i of particle i over time t by implementing the integration method of Ermak,³⁷

$$\mathbf{r}_i(t + \delta t) = \mathbf{r}_i(t) - \frac{\delta t}{\xi} \nabla U_i(t) + \delta \mathbf{r}_i^G + \delta t \dot{\gamma}(t) z_i(t) \hat{\mathbf{x}}, \quad (3)$$

with δt being the integration time step, $-\nabla U_i(t)$ being the force on particle i determined by the sum of all colloid–colloid and colloid–wall interactions, $\xi = k_B T/D_0$ being the friction coefficient with D_0 the particle short-time self-diffusion constant, and $\delta \mathbf{r}_i^G$ a random displacement sampled from a Gaussian distribution with zero mean and variance $\langle (\delta r_{i\alpha}^G)^2 \rangle = 2D_0 \delta t$ and $\alpha \in \{x, y, z\}$. Finally, the term $\dot{\gamma}(t) z_i(t) \hat{\mathbf{x}}$ imposes a linear velocity profile on

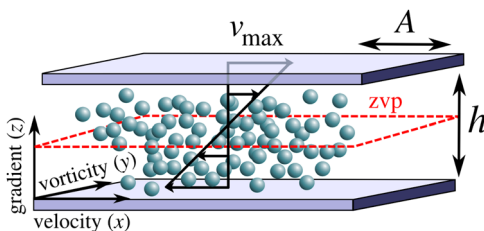


FIG. 1. Schematics of the system. Long-range repulsive colloidal particles (blue spheres) are confined in z by the presence of two soft repulsive planar walls at $z = 0$ and $z = h$. The walls move in opposite directions along x with an oscillatory motion, characterized by amplitude A and frequency of oscillation f . The shear induces the formation of a linear velocity profile on the system, represented here by black arrows. Particles are not subjected to any flow drag in the zero velocity plane (zvp), shown with a red dashed line.

the system in order to account for the oscillating shear. Here, $\dot{\gamma}(t) = \dot{\gamma}_{\max} \cos(2\pi ft)$ denotes the shear rate, which is dependent on the maximum shear rate $\dot{\gamma}_{\max}$ and the frequency of oscillations f . Note that the Gaussian displacement determines the diffusive motion of the particle, while the displacement along x , corresponding to the shear direction, is responsible for the formation of a velocity profile in the colloidal fluid, which depends linearly on the particle height $z_i(t)$. A previous experimental study³⁸ showed that the velocity profile deviates from linearity in the presence of crystal domains or randomly stacked hexagonal planes in the system. In the proximity of these regions, the shear rate is 1.5 times larger than the one measured in the fluid phase. Despite this, we neglect possible deviations from the linear flow profile, since we believe that they should not have a strong influence on the structures that we observe after applying oscillatory shear.

We investigate the out-of-equilibrium phase behavior of the system under external oscillatory shear, where we independently tune the frequency f and maximum strain amplitude γ_{\max} of the oscillations. The latter quantity is defined by $\gamma_{\max} = 2A/h$, where A is the amplitude of the oscillation and $h/2$ is the height of the wall from the zero velocity plane (zvp), illustrated in Fig. 1 by a red dashed line. The previously defined maximum shear rate $\dot{\gamma}_{\max}$ is related to f and γ_{\max} via the relation $\dot{\gamma}_{\max} = 2\pi f \gamma_{\max}$.

We simulate a system of $N \simeq 3000$ charged colloidal particles in a box with dimensions $L_x \times L_y \times L_z = 32 \times 32 \times 18\sigma^3$ and with periodic boundary conditions in the x - and y -directions. The colloids interact with a long-range repulsive Yukawa interaction characterized by a Debye screening length of $1/\kappa\sigma = 0.5$ in order to model a long-range repulsion between the particles, which is small enough that the interaction energy becomes negligible at the largest distances in our simulation box. We choose a cutoff distance of $r_{\text{cut}} = 0.5L_x$, where L_x is the smallest dimension with periodic boundary conditions. The potential energy of two particles at a distance r_{cut} is very small and measures $\beta U(r_{\text{cut}}) = 5 \times 10^{-13}$. We set $\delta t = 10^{-4} \tau_B$ and $\xi = 4 k_B T \tau_B / \sigma^2$, where $\tau_B = \sigma^2 / D_0$ is the Brownian relaxation time. Finally, we define the Péclet number $\text{Pe} = \dot{\gamma}_{\max} \eta \sigma^3 / (8k_B T) = f \tau_B \gamma_{\max} / 3$, where η is the shear viscosity of the solvent.

B. Local structure analysis

We study the formation of out-of-equilibrium ordered structures in colloidal fluids under oscillatory shear. We analyze the oscillatory shear-induced structures with varying methods, which we describe in this section.

As a preliminary investigation, we compute the radial distribution function $g(r) = \langle \sum_{i,j \neq i}^N \delta(r - |\mathbf{r}_i - \mathbf{r}_j|) \rangle / (N\rho)$, where $\mathbf{r}_{i,j}$ are the position vectors of particle i and j , $\rho = N/V$ is the number density with N the number of particles and V the volume, and the angular parentheses indicate an ensemble average. The expression above is valid in homogeneous and isotropic systems. The latter condition does not hold in our system due to the presence of the confining walls orthogonal to z . Therefore, we cannot merely normalize the quantity $\langle \sum_{i,j \neq i}^N \delta(r - |\mathbf{r}_i - \mathbf{r}_j|) \rangle$ by a constant ideal gas density ρ . On the contrary, we compute the radial distribution of N^{ig} ideal gas particles confined in the same simulation box, thus obtaining the correctly normalized radial distribution function for our system,

$$g(r) = \frac{\left\langle \sum_{i,j \neq i}^N \delta(r - |\mathbf{r}_i - \mathbf{r}_j|) \right\rangle}{\left\langle \sum_{i,j \neq i}^N \delta(r - |\mathbf{r}_i^{\text{ig}} - \mathbf{r}_j^{\text{ig}}|) \right\rangle} \left(\frac{N^{\text{ig}}}{N} \right)^2, \quad (4)$$

where $\mathbf{r}_{ij}^{\text{ig}}$ indicates the position vector of the ideal gas particle i or j .

The radial distribution function of long-range repulsive systems presents quite broad peaks due to the softness of the interaction potential, so this method is not sufficiently accurate to distinguish the different crystal structures. To this end, we use the bond-orientational order parameters,^{39,40} which enable us to identify different crystal structures on a single particle level. In particular, we implement the version reported by Lechner and Dellago.⁴¹ This algorithm classifies the environment of each particle as described by the local arrangement of its neighbors $N_b(i)$. The algorithm associates to each particle i , a complex vector $q_{lm}(i)$ defined by

$$q_{lm}(i) = \frac{1}{N_b(i)} \sum_{j=1}^{N_b(i)} Y_{lm}(\mathbf{r}_{ij}), \quad (5)$$

where l is a free integer parameter, m is an integer defined in the range $-l \leq m \leq l$, and $Y_{lm}(\mathbf{r}_{ij})$ denotes the spherical harmonics. The distance vector $\mathbf{r}_{ij} = \mathbf{r}_i - \mathbf{r}_j$ connects particle i to particle j , and the sum is performed over the first shell of neighbors, which counts all particles j within a radial cutoff distance of particle i . We set the cutoff distance equal to the position of the first minimum of the radial distribution function of the system. In order to quantify the correlation of the local environments surrounding particle i and j , we calculate the scalar product

$$\zeta_l(i, j) = \frac{\sum_{m=-l}^l q_{lm}(i) q_{lm}^*(j)}{\left(\sum_{m=-l}^l |q_{lm}(i)|^2 \right)^{1/2} \left(\sum_{m=-l}^l |q_{lm}(j)|^2 \right)^{1/2}}, \quad (6)$$

where the symbol $*$ indicates the complex conjugate. We define particles i and j to be connected if $\zeta_l(i, j) > 0.6$. Finally, particle i belongs to a crystal-like environment if $n_c \geq 8$, where n_c is the number of connections. If this is the case, we label it solid-like, otherwise liquid-like. We perform this analysis by using $l = 6$ because of the hexagonal symmetry of the observed crystals. Along the lines of Ref. 41, we compute the average bond-orientational order parameters defined by

$$\bar{q}_{lm}(i) = \frac{1}{\tilde{N}_b(i)} \sum_{k=0}^{\tilde{N}_b(i)} q_{lm}(k), \quad (7)$$

where the sum is performed over the neighbors of particle i plus particle i itself, thus leading to $\tilde{N}_b(i) = N_b(i) + 1$. Beyond identifying the crystalline particles as described above, we also like a way to distinguish the different crystal structures. A system of hard-core Yukawa particles can either form body-centered-cubic (bcc) or face-centered-cubic (fcc) crystal structures, depending on the volume fraction of the system and the specific parameters that characterize the pair interaction potential, e.g., the Debye screening length $1/\kappa\sigma$ and the charge on the colloidal surface.³⁵ On the basis of previous

experimental and numerical studies, we expect that the application of an external oscillatory shear might promote the formation of any of the aforementioned crystal structures. In order to identify the different crystal structures, we also employ the rotational invariant cubic averaged bond-order parameter

$$\bar{w}_l(i) = \frac{\sum_{m_1+m_2+m_3=0} \binom{l}{m_1} \binom{l}{m_2} \binom{l}{m_3} \bar{q}_{lm_1}(i) \bar{q}_{lm_2}(i) \bar{q}_{lm_3}(i)}{\left(\sum_{m=-l}^l |\bar{q}_{lm}(i)|^2 \right)^{3/2}}, \quad (8)$$

where the term in parentheses is the Wigner 3-j coefficient,⁴² and the sum runs over all possible combinations of $m_k \in \{-l, l\}$, which satisfy the relation $\sum_{k=1}^3 m_k = 0$. To be more specific, we use the \bar{w}_6 order parameter to discriminate whether a solid-like particle belongs to a bcc crystal indicated by $\bar{w}_6 > 0$ or belongs to an fcc or hexagonal-close-packed (hcp) crystal in the case of $\bar{w}_6 < 0$. We further distinguish the two structures by computing \bar{w}_4 , which gives $\bar{w}_4 < 0$ for a fcc and $\bar{w}_4 > 0$ for an hcp crystal. In order to minimize the error caused by the presence of the boundaries in z , we exclude the top and bottom layers from the computation of the local bond-order parameter, while we exclude the second top and second bottom layers from the computation of the average bond-order parameters. The full bond-order parameter analysis was done on ~ 2000 particles distributed over seven layers.

Ultimately, we compute the diffraction pattern of different crystal planes in order to further characterize the crystal structure and its orientation with respect to the direction of shear. We first collect configurations of the system at specific times within every period of oscillation. We analyze configurations obtained at $\gamma(t) = 0$ and $\gamma(t) = \pm A$, which correspond to the instantaneous zero strain amplitude (the walls are aligned) and instantaneous maximum strain amplitude (the walls are in opposite positions), respectively. This enables us to investigate the structure of the system at different moments of the oscillatory shear cycle and identify the transformation mechanism between different structures over time. To this end, we average over about 100 configurations, which were collected at the same period within the oscillation cycle, after a fixed number of cycles. We analyze the averaged configurations, identify the crystal planes, and determine their structure. With this procedure, we reduce the statistical noise due to thermal fluctuations, which is more pronounced in the case of long-range interacting systems as compared to hard spheres.¹⁶ Finally, we also compute the structure factor $S(q)$, which is defined by

$$S(q) = \frac{1}{N} \left\langle \sum_{j=1}^N \sum_{k=1}^N e^{iq(\mathbf{r}_k - \mathbf{r}_j)} \right\rangle, \quad (9)$$

where i denotes the imaginary unit. The angular parentheses indicate an ensemble average and \mathbf{q} is a vector in reciprocal space chosen such that $q_\alpha = 2\pi n/L_\alpha$, with n an integer, $\alpha \in \{x, y, z\}$, and L_α the simulation box dimension.

III. RESULTS AND DISCUSSION

We start the simulation runs with an initial configuration of the system in the equilibrium fluid phase at a packing fraction

$\phi = \pi\sigma^3 N/6V = 0.085$ just below the fluid-bcc freezing density $\phi_f = 0.092$.³⁵ We apply external oscillatory shear and perform simulations for different values of the oscillation frequency $1 \leq f\tau_B \leq 100$ and maximum strain amplitude $0.1 \leq \gamma_{\max} = 2A/h \leq 2$. Comparing the amplitude A with the averaged distance between the particles $\rho^{-1/3}$, we find that this range of maximum strain amplitudes corresponds to an amplitude of $0.5\rho^{-1/3} \leq A \leq 9\rho^{-1/3}$ for a system with $h = L_z = 18\sigma$. The formation of a crystal structure occurs after the application of shear for a number of oscillations, which varies with frequency f . As a general trend, this number increases upon increasing f and varies from a minimum of 200 until a maximum of ~ 3000 oscillations. As the initial equilibrium structure is near the fluid-bcc freezing transition, we expect to observe crystallization of a bcc structure upon the application of shear. Intriguingly, we find a sliding layer phase, a string phase, and a twinned fcc phase. As the twinned fcc phase is rather surprising and unexpected, we perform a detailed analysis of the martensitic fcc phase transition below. Note that the crystal structures formed via application of shear are out-of-equilibrium structures, i.e., we observe the melting of each identified ordered structure upon cessation of shear.

A. Twinned fcc and bcc-fcc martensitic transformation

Previous studies have already shown that a hard-sphere fluid close to the freezing density forms a twinned fcc phase when sheared with a maximum strain amplitude of $\gamma_{\max} \simeq 0.35$.^{12,13,16,18,43} Around this value, convective flows enhance collisions between particles and the fluid transitions into a crystal structure, most likely to minimize the stress.

For the long-range repulsive system under investigation here, we also observe a transition from a fluid to an ordered structure when we apply oscillatory shear with a maximum strain amplitude of $\gamma_{\max} \simeq 0.35$ in a wide range of frequencies $3/\tau_B < f < 100/\tau_B$, corresponding to a Peclet number range of $0.35 < Pe < 11.7$. To illustrate this, we plot the radial distribution function $g(r)$ of a system sheared with $\gamma_{\max} = 0.35$ and $f = 60.0/\tau_B$ ($Pe = 7$) at the zero strain amplitude (red) and maximum strain amplitude $\pm A$ (light green and dark green) in Fig. 2 along with the $g(r)$ of a quiescent fluid (black) as measured before applying oscillatory shear.

We obtain the respective radial distribution functions by averaging over 350 configurations selectively collected at zero and maximum ($\pm A$) strain amplitudes, respectively. The $g(r)$'s at zero and maximum strain amplitudes display peaks that differ in position and shape from the $g(r)$ observed for a quiescent fluid. These differences indicate a change in structure after applying shear. Note that the $g(r)$'s at zero and maximum strain amplitudes also differ from each other, suggesting that the two structures are different. The $g(r)$'s obtained at the maximum strain amplitude $\pm A$ are very similar, revealing the formation of the same structure at the two extremes of the oscillation. This analysis offers only a preliminary understanding of the local particle arrangement. In fact, a one-to-one comparison of the peak positions of the $g(r)$ with perfect crystals is prevented by the broadness of the peaks, which is caused by the softness of the repulsive pair interaction in combination with a low particle density.

To characterize the shear-induced crystals, we perform a bond-orientational order analysis as presented in Fig. 3. We compute the

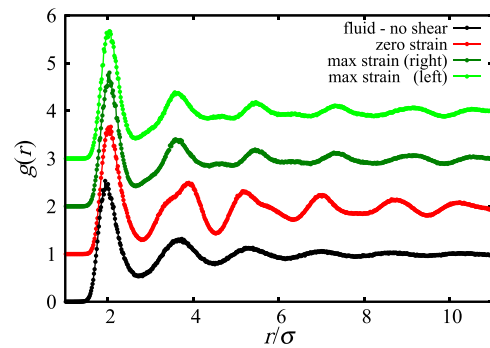


FIG. 2. Radial distribution function $g(r)$ of a system consisting of long-range repulsive charged colloids before (black) and after the application of shear with the maximum strain amplitude $\gamma_{\max} = 0.35$ and frequency of oscillation $f = 60.0\tau_B^{-1}$ ($Pe = 7$). We selectively analyze configurations at zero strain amplitude (red) and maximum amplitude of oscillation $\pm A$ (light green and dark green).

averaged \bar{q}_6 bond-order parameter in order to identify the crystalline particles. We further compute the \bar{w}_6 order parameter to identify crystalline particles that belong to a bcc environment and mark them red. Finally, the \bar{w}_4 order parameter distinguishes between fcc and hcp particles, which we visualize in green and blue, respectively. We display three instantaneous configurations of the system (zoomed-in) taken at $\gamma = -A, 0, A$ from the left to the right in Fig. 3(a). We observe that shear induces the formation of an fcc-like structure at the two extremes of the oscillation, as demonstrated by the dominant presence of green particles as compared to red and blue. This structure deforms during a shearing cycle and transforms into a bcc-like crystal at the zero strain amplitude, where the number of red particles exceeds the number of green and blue particles. We illustrate a scatter plot of the system in the \bar{w}_4 - \bar{w}_6 plane in Fig. 3(b). Each plot shows the results obtained by averaging over 100 configurations collected at the aforementioned strain amplitudes. For $\gamma = \pm A$, the cloud mostly covers the region characterized by $\bar{w}_6 < 0$ and $\bar{w}_4 < 0$, which denotes the formation of an fcc-like crystal. We color the points that fall in this region in green, while those which fall in the other two regions, denoted as “hcp” and “bcc” are colored in blue and red, respectively. We observe that the cloud is composed of these two colors as well, but in minor quantity, indicating the presence of some defects associated with bcc-like and hcp-like structures. As the walls move back to the resting position of the zero strain amplitude, the cloud progressively migrates toward the positive axis of \bar{w}_6 , reaching the peak position at $\bar{w}_6 = 0.01$ for $\gamma = 0$.

We visualize this continuous transition from the fcc-like into the bcc-like phase by monitoring the crystallinity fraction of each crystal structure over time. The crystallinity fraction χ of a particular crystal is defined by the number fraction of particles that belong to that crystal structure. We report χ for the bcc, fcc, and hcp crystals as represented with red, green, and blue points, respectively, in Fig. 3(c). We show χ for one period of oscillation, starting from $\gamma = 0$, where $\chi = 1$ for bcc and $\chi = 0$ for fcc and hcp. We observe that the fraction of hcp crystal is quite low for the entire period of oscillation, reaching a maximum of $\chi \simeq 0.09$ at $\gamma = \pm A$. On the other hand,

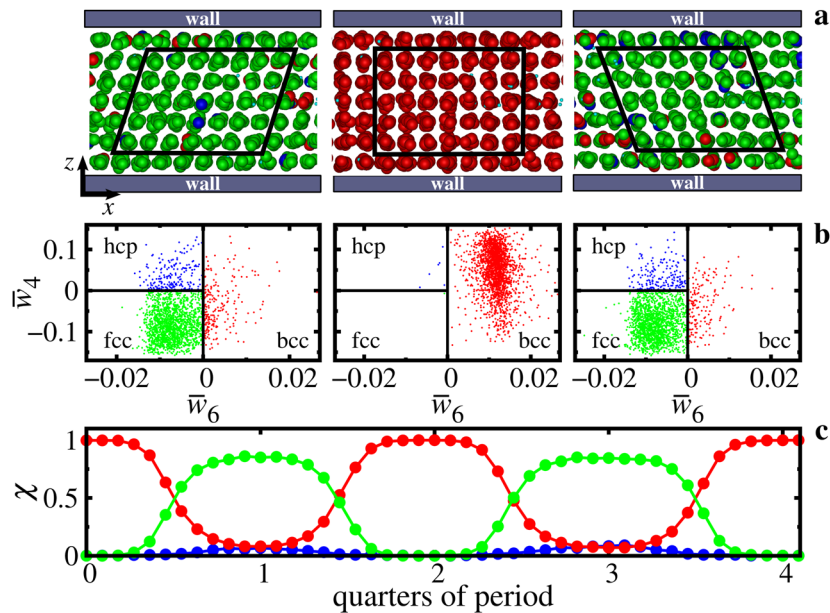


FIG. 3. Analysis of the bond-orientational order parameters of the twinned fcc phase in a system consisting of long-range repulsive charged colloids under external oscillatory shear with a maximum strain amplitude of $\gamma_{\max} = 0.35$ and frequency of oscillation of $f = 60.0\tau_B^{-1}$ ($Pe = 7$). (a) Sequence of three snapshots (zoomed-in) taken at the maximum strain amplitude $\pm A$ (left and right) and zero strain amplitude (center). Particles that belong to the fcc, hcp, and bcc crystals are colored in green, blue, and red, respectively. Fluid particles are colored in cyan and reduced in diameter to enhance visualization. (b) Scatter plot of the system in the \bar{w}_4 - \bar{w}_6 plane. We identify bcc particles if $\bar{w}_6 > 0$ and fcc particles if $\bar{w}_4 < 0$. Each plot represents the system in a moment of the oscillation cycle corresponding to the snapshot above it. Points are color-coded as in (a), according to the region they fall into. (c) Crystallinity fraction of bcc (red), fcc (green), and hcp (blue) as a function of time in one period of oscillation.

the χ values for the bcc and fcc crystals oscillate counter-phase from zero to one.

To summarize, the radial distribution function and the bond-orientational order analysis reveal the formation of two different crystals, namely, an fcc-like structure at maximum strain amplitude that transforms continuously via a martensitic transition into a bcc-like structure at zero strain amplitude.

In order to identify the phase transformation mechanism of the oscillatory shear-induced bcc–fcc transition, we identify the underlying unit cell of the two structures and the orientation of the crystals with respect to the shearing plane. We, therefore, proceed by slicing single crystal planes and calculating the respective diffraction patterns. In Fig. 4, we show three different crystal planes of the bcc-like structure, together with the diffraction pattern and a schematics.

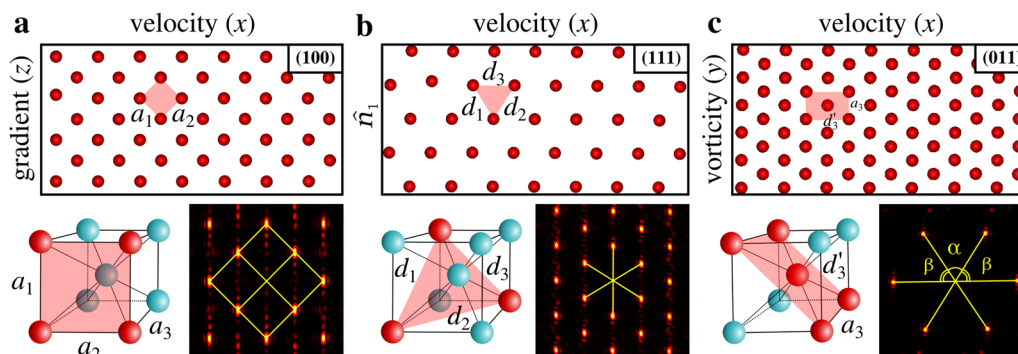


FIG. 4. Different crystal planes and diffraction patterns for the twinned fcc phase obtained at zero strain amplitude under external oscillatory shear characterized by $\gamma_{\max} = 0.35$ and $f = 60/\tau_B$ ($Pe = 7$). The schematics highlights the plane in a body-centered tetragonal unit cell. (a) (100) plane oriented parallel to the velocity–gradient plane. (b) (111) plane oriented parallel to the vorticity– \hat{n}_1 plane. The unit vector \hat{n}_1 forms an angle of 52.6° with the gradient–velocity plane. (c) (011) plane oriented parallel to the velocity–vorticity plane (walls).

The latter represents the more generic body-centered tetragonal (bct) unit cell, where we indicate the lattice constants a_1 , a_2 , and a_3 and highlight the plane under examination with a red color. In Fig. 4(a), we display the (100) plane, which forms parallel to the velocity–gradient plane, with lattice constants a_1 and a_2 rotated by 45° with respect to the z and x axes, respectively. This feature is visible by comparing the highlighted region in the velocity–gradient plane and in the unit cell. The diffraction pattern exhibits bright spots with a small elongation along z , which is a consequence of the smaller system size in z as compared to x .

The diffraction spots show a four-fold symmetric pattern and are positioned on the vertices of perfect squares, forming angles of 90° . This aspect reflects the orthogonality between the lattice vectors \mathbf{a}_1 and \mathbf{a}_2 . We measure the lattice spacings and obtain $a_1/\sigma = 2.41 \pm 0.02$ and $a_2/\sigma = 2.40 \pm 0.02$, which are in very good agreement with each other, and hence, we find within our statistical accuracy that the two lattice constants $a_1 \simeq a_2 = a$. We retrace the orientation of the (111) plane by rotation. We face the (100) plane as oriented in Fig. 4(a) and rotate the system about x by 52.6° . This value is remarkably close to the angle formed by the intersection of the (100) and (111) planes in a perfect bcc crystal, which is 54.7° . We show the (111) plane in Fig. 4(b) and recognize two important features that characterize also the (111) plane in a perfect bcc crystal. The first one is the arrangement of particles in a hexagonal pattern, and the second one is the visibly lower particle density as compared to other planes such as the (100) and (011) shown in Fig. 4. The diffraction pattern shows hexagonal symmetry, giving a spot-center-spot average angle of $60^\circ \pm 3^\circ$. We measure the face diagonal $d_3/\sigma = 3.43 \pm 0.02$, which is in very good agreement with a perfect bcc face diagonal $\sqrt{2}a/\sigma = 3.40$ with a the lattice constant. We also measure $d_1/\sigma = 3.29 \pm 0.01$ and $d_2/\sigma = 3.27 \pm 0.01$, which also agree well with each other, but less with d_3 . This feature might indicate that the lattice constant a_3 slightly differs from a . In order to verify this, we locate the (011) plane by further rotating the crystal around x by 37.4° from the (111) plane. This also implies that the intersection of the planes (100) and (011) forms an angle of 90° , so \mathbf{a}_3 is orthogonal to \mathbf{a}_1 and \mathbf{a}_2 , in line with a bct crystal, where the lattice vectors are all

orthogonal to each other. We illustrate the (011) plane in Fig. 4(c). This plane shows the highest particle density as also observed for a bcc crystal and is oriented parallel to the walls. This preferred orientation of the bcc crystal has already been observed in previous experimental work, where a strongly repulsive fluid in confinement crystallizes in a bcc structure with the (110) plane parallel to the walls,^{21,44} and can be explained by the fact that the close-packed plane usually has the lowest surface tension. The diffraction pattern shows six bright spots with two angles $\alpha = 65.6^\circ \pm 0.2^\circ$ and four angles $\beta = 57.0^\circ \pm 0.8^\circ$, as indicated in Fig. 4(c). In the (011) plane of a perfect bcc, particles form a pattern that resembles a distorted hexagon, characterized by two angles $\alpha' = 70.5^\circ$ and four angles $\beta' = 54.7^\circ$. We observe that α and β differ by a few degrees to α' and β' , respectively. This difference is determined by the length of $a_3/\sigma = 2.20 \pm 0.07$, which is slightly smaller than a . The face diagonal d'_3 is parallel to the velocity direction and coincides with the face diagonal d_3 of Fig. 4(b). As expected, we obtain $d'_3 = 3.42 \pm 0.02$, which is in good agreement with d_3 .

This analysis has further characterized the aforementioned bcc-like structure, which we now classify as a bct crystal with $a_3/a = 0.92$. Note that this ratio is lower, but relatively close to 1, which is the ratio of lattice constants for a perfect bcc crystal.

In a similar way, we analyze the fcc-like structure at the maximum strain rate. In Fig. 5, we show three different crystal planes of the fcc-like structure, together with the diffraction pattern and a schematics of the face-centered orthorhombic (fco) unit cell. The (110) plane forms parallel to the velocity–gradient plane, as shown in Fig. 5(a). We measure the lattice constant $b_3/\sigma = 2.85 \pm 0.03$ and the face diagonal $D_1/\sigma = 4.07 \pm 0.03$ from the diffraction pattern. The latter quantity is in good agreement with the face diagonal of an fcc with a lattice constant equal to b_3 , which is $\sqrt{2}b_3/\sigma = 4.04$. The angles measured from the diffraction pattern give an average of $90^\circ \pm 2^\circ$. From this orientation, we retrace the (001) plane by implementing two subsequent rotations, the first one about z by 90° and the second one about y by 36.3° . The (001) plane, shown in Fig. 5(b), is orthogonal to (110) and enables us to measure the lattice constants $b_1/\sigma = 2.93 \pm 0.02$ and $b_2/\sigma = 3.08 \pm 0.02$. The angles measured from

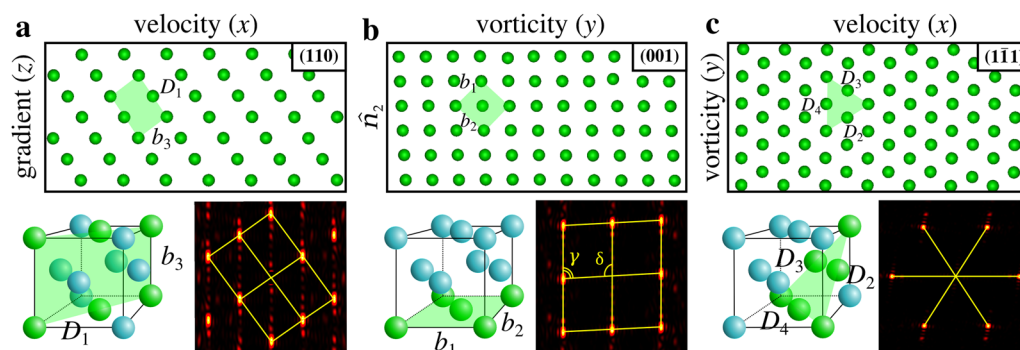


FIG. 5. Different crystal planes and diffraction patterns for the twinned fcc phase obtained at the maximum strain amplitude under external oscillatory shear characterized by $\gamma_{\max} = 0.35$ and $f = 60/\tau_B$ ($Pe = 7$). The schematics highlights the plane in a face-centered orthorhombic (fco) unit cell. (a) (110) plane oriented parallel to the velocity–gradient plane. (b) (001) plane oriented parallel to the vorticity– \hat{n}_2 plane. The unit vector \hat{n}_2 forms an angle of 36.3° with the gradient–vorticity plane. (c) (111) plane oriented parallel to the velocity–vorticity plane (walls).

the diffraction pattern show a small divergence from orthogonality, being $\gamma = 86.8^\circ \pm 0.6^\circ$ and $\delta = 93.2^\circ \pm 0.4^\circ$. Finally, we identify the (111) plane by rotating about y by 53.7° . The plane, shown in Fig. 5(c), is oriented parallel to the velocity–vorticity plane, with one of the close-packed directions almost perpendicular to x . Similar to the bcc-like crystal, we observe here also the formation of the densest plane parallel to the walls, which is in agreement with previous studies. We find that one close-packed direction is either parallel to y or it might form an angle of $\pm 9^\circ$ with respect to y . This feature is also observed in Ref. 16, where the authors apply oscillatory shear on a system of hard-sphere particles. We measure the face diagonals obtaining $D_2/\sigma = 4.1 \pm 0.02$, $D_3/\sigma = 4.07 \pm 0.02$, and $D_4/\sigma = 4.43 \pm 0.02$, where the first two are in good agreement with each other and the latter one is slightly larger, which is a direct consequence of b_2 being slightly larger than the other two lattice constants. The measured angles are on average $60.0^\circ \pm 4.5^\circ$, where the mean value of 60° reflects a coordination number of 6, and the standard deviation of 4.5° indicates a small deviation from the exact six-fold symmetry. This deviation corresponds to the one we measure in the (011) plane of the bcc-like structure. In fact, the two planes coincide as they are both oriented parallel to the velocity–vorticity plane, and the shearing mechanism affects only those interparticle distances that have a component in the gradient direction, leaving unchanged the interparticle distances in the velocity–vorticity plane.

On the basis of this analysis, we classify the fcc-like crystal as a face-centred orthorhombic (fco) structure since the angles from Figs. 5(a) and 5(b) are not exactly but nearly orthogonal and the unit cell displays three different lattice constants. Due to the small difference between b_1 , b_2 , and b_3 , with a maximum of $(b_2 - b_3)/b_3 = 0.08$, we consider this fco structure to be very close to an fcc.

In support of this, we visualize two adjacent fcc-like unit cells and identify the bct unit cell enclosed in them, as illustrated in Fig. 6(a), where particles forming the bct unit cell are highlighted in yellow. We estimate the ratio of the bct lattice constants $b_3/c = 1.34$, where $c = (D_1 + D_4)/4$, which indicates that the structure is relatively close to an fcc where the same ratio gives $\sqrt{2} \approx 1.41$ and differs from a bcc where the ratio is 1.

We explain the transformation mechanism from the bcc-like to the fcc-like unit cell in Figs. 6(b) and 6(c). Figure 6(b) shows a projection of the system in the velocity–vorticity plane, at the maximum strain amplitude (left and right) and zero strain amplitude (center). We illustrate a selection of 14 particles distributed in three adjacent z -stacked planes, where particles belonging to the bottom, middle, and top planes are colored gray, purple, and yellow, respectively. We observe the (111) planes stacked with an A–B–C structure in the left frame and its twinned structure stacked with an A–C–B fashion in the right frame. We increased the particle radius to enhance the visualization of the stacking sequence. The oscillatory shear-induced twinned fcc phase was already observed for hard spheres in 1988.¹² In our study, we also find the formation of this phase under oscillatory shear, but here, it occurs in a long-ranged strongly repulsive system at a volume fraction lower than that of the fluid–bcc freezing transition. The formation of this fcc structure is quite remarkable as this system in equilibrium is close to a fluid–bcc instead of a fluid–fcc phase transition. For this long-range repulsive system, the bcc structure is energetically more favorable than the fcc phase due to its lower number of nearest neighbors. Despite the energetic disadvantage, oscillatory shear preserves the formation of a twinned fcc phase even in long-ranged repulsive systems.

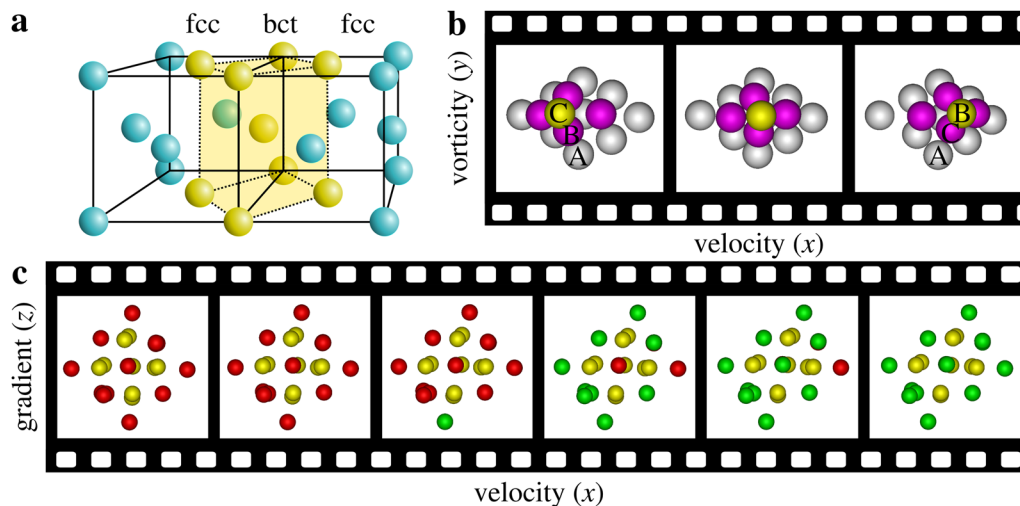


FIG. 6. (a) Schematics representing two adjacent fcc unit cells and the bct unit cell enclosed in them (yellow). (b) Sequence of snapshots showing 14 particles that belong to three adjacent z -stacked planes. We recognize the A–B–C stacking of the fcc structure in the left frame and its twinned phase in the right frame, where the stacking sequence changes to A–C–B. The middle frame shows the stacking of the planes at zero strain amplitude. The particle radius is increased to enhance the visualization of the stacking sequence. (c) Sequence of snapshots covering one quarter of the oscillation period from the zero strain amplitude (left) to the maximum strain amplitude (right). The yellow particles form a bct unit cell, which deforms with shear. The rest of the particles are colored according to whether they belong to a bcc-like (red) or an fcc-like (green) crystal.

We visualize the transformation from the bcc-like to the fcc-like unit cell in Fig. 6(c). Note that we restore the particle dimensions to their original size here. The sequence of snapshots shows a projection of the system on the velocity–gradient plane. The first frame to the left corresponds to the zero strain amplitude, while the last frame corresponds to the maximum strain amplitude such that the entire sequence covers a quarter of the oscillation period. We highlight in yellow the particles forming a bcc unit cell in the bcc-like structure (first frame) and a bcc unit cell in between two fcc-like unit cells (last frame) as in Fig. 6(a). Note that the remaining particles are colored in red or green depending on whether they belong to a bcc-like or an fcc-like crystal, respectively. Monitoring the system from this angle facilitates the visualization of how the unit cell progressively deforms over time. The square of highlighted particles in the first frame corresponds to the (100) plane in the bcc-like structure. The shear applied in the x – y plane continuously deforms this squared pattern, which eventually becomes a rectangle in the last frame. Here, the rectangle lies on the (110) plane of the fcc-like structure, and its surface area corresponds to half the surface area of the (110) plane in a fcc-like unit cell, as visible from Fig. 6(a). This transformation mechanism from this perspective bridges the two structures in a continuous fashion, providing an intuitive comprehension of the structure deformation process in its entirety.

B. Out-of-equilibrium phase diagram

Previous experimental and simulation studies showed that the formation of out-of-equilibrium structures is highly dependent on the maximum strain amplitude γ_{\max} and frequency of oscillation f of the applied external oscillatory shear. We, therefore, study the shear-induced structures that form in our long-range repulsive colloidal suspension as a function of maximum strain amplitude γ_{\max} and frequency of oscillation f . We first describe the structures that we observe upon the application of oscillatory shear, and finally, we summarize our results in an out-of-equilibrium phase diagram.

1. Fluid

For small values of γ_{\max} , the application of shear is not strong enough to induce a phase transformation in the fluid, irrespective of the frequency of oscillations f . In addition, larger values of γ_{\max} prevent the formation of any ordered structures, due to the large number of effective collisions between the particles. Note that in a long-range repulsive colloidal suspension, particles never collide with their colloidal surfaces, but approach each other down to distances where the repulsive potential steeply rises. For simplicity, we refer to these events as “effective collisions” among long-range interacting colloids in order to distinguish them from the collisions between hard spheres. We display a typical configuration of the system after the application of shear with $\gamma_{\max} = 0.05$ and $f = 1\tau_B^{-1}$ ($Pe = 0.017$) in Fig. 7(a). In addition, we present the density distribution $\rho(z)$ along z of the system before (red) and after (blue) the application of shear with $\gamma_{\max} = 0.05$ and $f = 1\tau_B^{-1}$ ($Pe = 0.017$) in Fig. 7(b). We observe that the density profiles exhibit pronounced layering, especially close to the walls and after the application of shear. We, thus, conclude that the layering is mainly caused by the confinement rather than by shearing. We further confirm the

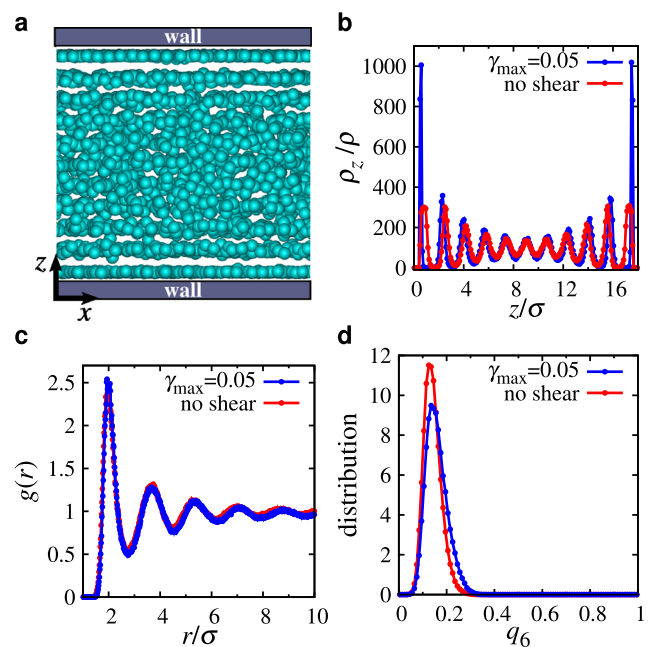


FIG. 7. Structural properties of a long-range repulsive colloidal suspension before (red line) and after (blue line) the application of oscillatory shear with $\gamma_{\max} = 0.05$ and $f = 1\tau_B^{-1}$ ($Pe = 0.017$). (a) Typical configuration of the system after shear. (b) Normalized density distribution $\rho(z)$ as a function of z . (c) Radial distribution function $g(r)$. (d) Probability distribution function of the averaged \bar{q}_6 bond-order parameter for the fluid phase before and after shear.

fluid nature of the system by analyzing the radial distribution function $g(r)$ and the \bar{q}_6 probability distribution function in Figs. 7(c) and 7(d), respectively. We compare the distributions obtained by analyzing the system before and after applying shear, represented here by the red and blue lines, respectively. The radial distribution functions are nicely superimposed and present the typical density oscillations in a fluid phase. The situation is similar for the \bar{q}_6 bond-order parameter, where the blue and red probability distributions display a maximum at $\bar{q}_6 \sim 0.15$, which is below the peak of the bcc probability distribution at $\bar{q}_6 \sim 0.35$, thereby confirming that the system is in the fluid phase. Additionally, for strain amplitudes $\gamma_{\max} \gtrsim 1.5$, we again find that the system remains in a disordered fluid phase upon application of oscillatory shear independent of the frequency of oscillation. We did not explore the regime of higher strain.

2. Twinned fcc-bcc martensitic transformation

In Sec. III A, we have already shown that this system under external oscillatory shear with $\gamma_{\max} \approx 0.35$ favors the formation of an fcc crystal. The reason why the fluid-fcc transition is triggered by $\gamma_{\max} = 0.35$ is fully explained by geometrical considerations of the fcc structure. Consider an fcc unit cell of lattice constant a and a hexagonal plane, where particles occupy the lattice positions “A.” The hexagonal layer above it could occupy either the neighboring

void “B” or “C,” whose reciprocal distance is $2\Delta x = a/\sqrt{6}$. The distance between two adjacent hexagonal planes is $\Delta z = a/\sqrt{3}$, and the ratio $\Delta x/\Delta z \approx 0.35$ is equal to the value of γ_{\max} that determines the formation of an fcc crystal. In fact, the quantity $2\Delta x$ represents the distance covered by a particle with respect to the hexagonal layer below it in half an oscillation cycle; therefore, $\gamma_{\max} = 0.35$ enables the switching mechanism from A–B–C stacking to A–C–B stacking, as we have previously illustrated in Fig. 6(b).

3. Sliding layers and strings

For maximum strain amplitudes $\gamma_{\max} \gtrsim 0.6$, the effective collisions between the particles prevent the formation of a twinned fcc structure, which is confirmed by a bond-order parameter analysis that shows that $\bar{w}_6 > 0$ during the entire oscillation cycle. The system rather forms a string phase or a sliding layer phase, depending on the frequency of oscillations. The sliding layer phase is composed of hexagonal planes parallel to the velocity–vorticity plane with a close-packed direction parallel to the velocity direction, which is different from what we have seen for the twinned fcc structure, which is characterized by hexagonal planes in the velocity–vorticity plane but with the close-packed direction perpendicular to the flow direction. This orientation is particularly convenient for the system since it enables z -stacked hexagonal planes to freely slide on top of each other along the velocity direction. We show typical configurations of the sliding layer phase obtained for $\gamma_{\max} = 0.80$ and $f = 30\tau_B^{-1}$ ($Pe = 8$) in Fig. 8. The top panel shows a projection of the system in the vorticity–gradient plane. We observe that each third hexagonal plane is stacked on top of the first one. From this angle, we clearly see that each layer easily slides within the grooves of the layers above and below it, while the system is sheared perpendicularly to this plane. We visualize crystalline particles with $\bar{w}_6 > 0$ in red, while those characterized by $\bar{w}_6 < 0$ and $\bar{w}_4 > 0$ or $\bar{w}_4 < 0$ in blue or green, respectively. We reduce the radius of liquid-like particles, represented in cyan here. The bond-orientational parameter analysis gives a crystallinity fraction of 90%, and mostly $\bar{w}_6 > 0$. We select one of the z -stacked planes, specifically the zero-velocity plane, and show it in the velocity–vorticity representation in the bottom panel. Here, all particles are illustrated with the same color and radius in order to enhance the visualization of the pattern they form in the plane. We compute the diffraction pattern, which displays a six-fold symmetry, thus proving that the particles form a hexagonal arrangement. Moreover, we quantify the hexagonal order in the plane by computing the 2D local bond-order parameter ψ_6 given by

$$|\psi_6(j)| = \left| \frac{1}{n_c(j)} \sum_{k=1}^{n_c(j)} e^{i6\theta(\mathbf{r}_{jk})} \right|, \quad (10)$$

where j is a particle in the plane at \mathbf{r}_j and the sum runs over the $n_c(j)$ nearest neighbors of particle j . $\theta(\mathbf{r}_{jk})$ is the angle between the vector $\mathbf{r}_{jk} = \mathbf{r}_k - \mathbf{r}_j$ and an arbitrarily chosen reference vector. The number of nearest neighbors $n_c(j)$ is defined as the number of particles whose distance with j is smaller than a threshold r_{ψ_6} . We choose $r_{\psi_6} = 2.8\sigma$ corresponding to the first minimum in the radial distribution function. We then compute the global bond-order parameter Ψ_6 defined as the average ψ_6 value,

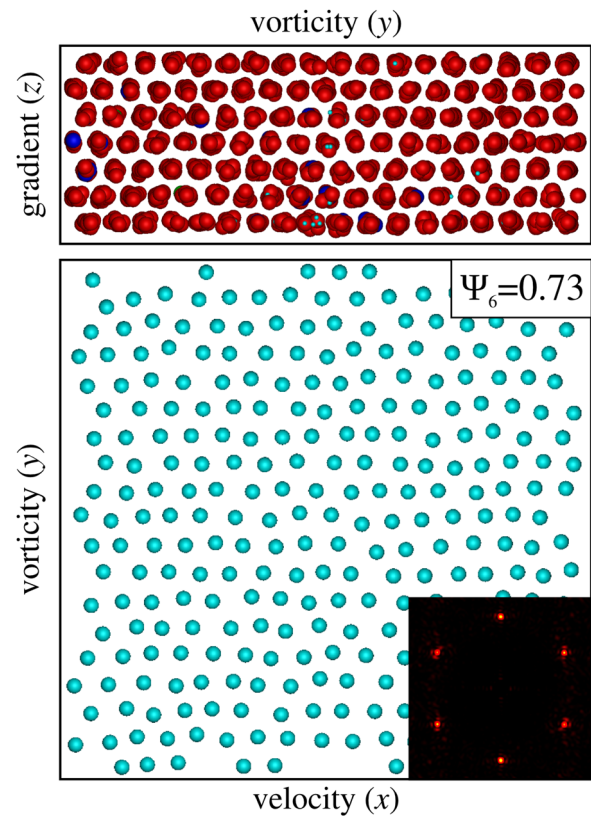


FIG. 8. A typical configuration of the sliding layer phase obtained at $\gamma_{\max} = 0.80$ and $f = 30\tau_B^{-1}$ ($Pe = 8$). The top panel shows a projection of the system in the vorticity–gradient plane. The system is composed of crystalline particles with $\bar{w}_6 > 0$, as denoted in red. The stacking of xy planes is such that every third layer sits on top of the first one. The bottom panel shows the zero velocity plane, exhibiting hexagonal order as demonstrated by the high value of Ψ_6 and the six-fold symmetry of the corresponding diffraction pattern.

$$\Psi_6 = \left| \frac{1}{N_p} \sum_{j=1}^{N_p} \psi_6(j) \right|, \quad (11)$$

where N_p is the number of particles in the plane. Note that Ψ_6 is equal to 1 in a perfect hexagonal plane, while it vanishes in a fluid phase. We obtain $\Psi_6 = 0.73$ for the plane displayed in Fig. 8, thereby confirming a high hexagonal order.

Previous studies reported the formation of a string phase for high values of γ_{\max} and low frequency of oscillation f .²³ The string phase is similar to the sliding layer phase when observed from the vorticity–gradient representation. In fact, high values of γ_{\max} make the stacking described in Fig. 8 still favorable. The main difference that distinguishes the string phase from the sliding layer phase is the lack of hexagonal order in the velocity–vorticity plane. The string phase rather forms strings of particles parallel to the velocity direction. This difference is probably caused by a lower ratio of convective diffusion with respect to thermal diffusion that reduces the amount of hexagonal order in the plane. We also find the string phase for $\gamma_{\max} = 0.8$ and $f = 1\tau_B^{-1}$ ($Pe = 0.27$) and report it in Fig. 9. The

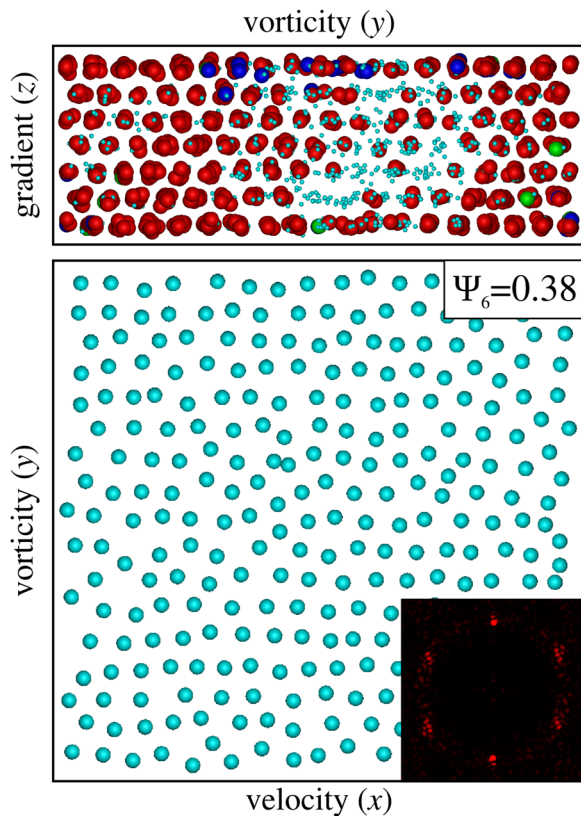


FIG. 9. Typical configuration of the string phase obtained at $\gamma_{\max} = 0.8$ and $f = 1\tau_B^{-1}$ ($Pe = 0.27$). The top panel shows a projection of the system in the vorticity–gradient plane. The system is composed of crystalline particles with $\bar{w}_6 > 0$ and fluid particles, denoted by red and cyan, respectively. The stacking of xy planes is such that every third layer sits on top of the first one. The bottom panel shows the zero velocity plane, showing string formation parallel to x , as also indicated by the corresponding diffraction pattern. The in-plane hexagonal order is quite low, as evidenced by a low Ψ_6 .

top panel shows a projection of the system in the vorticity–gradient plane. We find the same stacking sequence already observed for the sliding layer phase. Although, the crystallinity fraction of the system reaches only 45%, thus revealing less six-fold bond-orientational order with respect to the sliding layers. The zero-velocity plane is shown in the bottom panel of Fig. 9. Visual inspection reveals a low six-fold symmetry, which is confirmed by a low value of $\Psi_6 = 0.38$. Furthermore, the diffraction pattern displays bright spots in the vorticity direction, which indicates the presence of regularly separated strings parallel to x and weaker diffraction spots in the other directions indicating less order.

4. Out-of-equilibrium phase diagram

We summarize our results described above in the out-of-equilibrium phase diagram of Fig. 10, where we independently vary the maximum strain amplitude γ_{\max} and frequency of oscillations f . As a general trend, we observe that γ_{\max} is the main parameter that

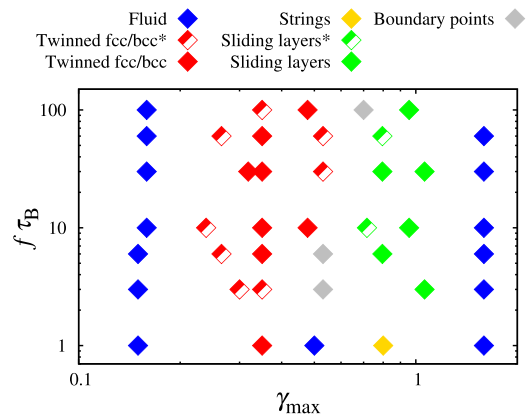


FIG. 10. Out-of-equilibrium phase diagram of a long-range repulsive colloidal suspension under oscillatory shear. Blue diamonds indicate the fluid phase, which is found for $\gamma_{\max} \lesssim 0.2$ and $\gamma_{\max} \gtrsim 1.5$. A twinned fcc via bcc martensitic transformation is observed for $0.25 \lesssim \gamma_{\max} \lesssim 0.5$ and represented here with red diamonds. The full state points display an fcc crystallinity fraction larger than 60%, while those half–full are characterized by an fcc crystallinity fraction smaller than 35%. Sliding layers are found for $0.75 \lesssim \gamma_{\max} \lesssim 1$ and represented here with green diamonds (half–full when sliding layers occupy only half the system size), while strings are found for only one yellow state point with $\gamma_{\max} = 0.80$ and $f = 1\tau_B^{-1}$ ($Pe = 0.27$). The gray diamonds are boundary state points with a crystalline structure that does not fully correspond to either the twinned fcc or the sliding layer phase.

triggers the formation of different phases, while f is rather irrelevant, except for the string phase that forms only for $f = 1\tau_B^{-1}$. The system remains in the fluid phase for $\gamma_{\max} \lesssim 0.2$ and $\gamma_{\max} \gtrsim 1.5$, as illustrated by the blue diamonds.

We observe the martensitic transformation between twinned fcc and bcc crystals in a wide region of the phase diagram, which covers $0.25 \lesssim \gamma_{\max} \lesssim 0.53$, as indicated by the red diamonds. However, these state points are not all equivalent to each other. We observe a well-defined fcc–bcc transformation mainly at $\gamma_{\max} \approx 0.35$, which we indicate with full red diamonds. For these state points, the fraction of the fcc crystal is above 60% at the extremes of the oscillation cycle. In the other cases, represented by half–full red diamonds, the system attempts to switch from bcc to fcc as passing from $\gamma = 0$ to $\gamma = \pm A$, but the fraction of the fcc crystal does not exceed 35%. This is likely due to the mismatch between γ_{\max} and the geometrical dimensions of the fcc structure, as explained above.

Furthermore, we observe the sliding layer phase for $0.75 \lesssim \gamma_{\max} \lesssim 1.1$ and $f \gtrsim 3\tau_B^{-1}$ ($0.75 \lesssim Pe \lesssim 1.1$) and the string phase for $\gamma_{\max} = 0.8$ and $f = 1\tau_B^{-1}$ ($Pe = 0.27$), which we report with green and yellow diamonds, respectively. We represent with half–full green diamonds those state points where the system forms a sliding layer phase in about half of the simulation box, while the remaining crystalline part of the system displays an orientation that we cannot identify with either of the previously identified structures.

Finally, note that gray diamonds represent boundary state points, where the system forms a crystalline structure whose orientation with respect to the simulation box does not fully correspond to either a twinned fcc/bcc nor a sliding layer phase. Finally, we wish to note that the sliding layer phase,^{4,45} the oscillating twinned fcc phase,^{4,45} and the string phase^{23,46} are also observed in simulations

using the Lees–Edwards periodic boundary conditions, i.e., without any walls, demonstrating that these structures are induced by oscillatory shear rather than the confinement.

IV. CONCLUSIONS

Using non-equilibrium Brownian dynamics simulations, we have investigated the out-of-equilibrium phase behavior of a long-range repulsive colloidal suspension under oscillatory shear. In contrast to previous simulation studies that only observed a shear-induced string phase in such a long-range repulsive system,²³ we demonstrate in this study that the formation of highly ordered structures is possible under oscillatory shear. Surprisingly, we discover that the twinned fcc phase, previously observed by shearing a hard-sphere fluid,^{12,16} also forms in a long-range repulsive system, when sheared with a maximum strain amplitude $0.25 \lesssim \gamma_{\max} \lesssim 0.5$.

We characterize the structures formed in this range of γ_{\max} by means of a bond-orientational order parameter and diffraction pattern analysis. The first method reveals the formation of an fcc-like crystal at the extremes of the oscillations and a bcc-like crystal at zero strain amplitude. We further inspect these structures via a diffraction pattern analysis, by which we identify the crystal unit cells and their orientation with respect to the direction of shear. The structure formed at the extremes of the oscillations is an fcc crystal as it displays three slightly different lattice constants. Nevertheless, these three lattice constants differ from each other by less than 8%. Therefore, we consider this fcc to be very close to an fcc crystal. The fcc is oriented with the densest plane (111) parallel to the walls, where one of the close-packed directions is orthogonal to the direction of shear x . The structure formed at the zero strain amplitude is a bct crystal with a lattice constant ratio of $a_3/a = 0.92$, which is very close to that of a bcc crystal. In addition, in this case, the densest plane (011) is parallel to the walls.

Finally, we retrace the transformation mechanism from bcc to fcc as the walls pass from the resting position of the zero strain amplitude to one of the extremes of an oscillation. We identify the continuous transformation between the two structures by following a bct unit cell from the velocity-gradient perspective at zero strain, during a quarter of a period of an oscillation. The bct unit cell, initially similar to a bcc unit cell, progressively deforms with increasing strain amplitude and elongates until it eventually fulfills the space of an fcc crystal at maximum strain amplitude.

For larger values of γ_{\max} , we also found other ordered structures. The sliding layer phase forms for $0.75 \lesssim \gamma_{\max} \lesssim 1$ and $f \geq 3\tau_B^{-1}$ ($Pe \geq 0.75$) and displays hexagonal planes parallel to xy with a close-packed direction parallel to the direction of shear x . The structure also shows the characteristic z -stacking from the vorticity-gradient projection, where each third layer sits on top of the first one. The string phase is observed for $\gamma_{\max} = 0.8$ and $f = 1\tau_B^{-1}$ ($Pe = 0.27$). Similar to the sliding layers, it displays the same z -stacking sequence in the vorticity-gradient plane. The string phase shows the formation of strings parallel to the direction of shear x , but differs from the sliding layer phase due to the lack of hexagonal order in the xy plane.

This work provided evidence that oscillatory shear induces the formation of 3D crystal structures also in a fluid of long-range repulsive colloids. The remarkable formation of an fcc crystal in

such a system, at low volume fraction, indicates the strength of this methodology, where specific flow-induced effective interactions enhance the mechanical stability of such a close-packed crystal below the freezing density of the system and favor the formation of an fcc over the thermodynamically more stable bcc structure. We, thus, find that the resulting oscillatory shear-induced phase behavior of an equilibrium fluid of long-range repulsive colloids just below the fluid-bcc phase transition resembles that of a fluid of hard-sphere colloids near the fcc freezing transition, and hence, the nearby stable solid phase does not seem to affect the shear-induced ordering. Even though we cannot rule out the possibility that hydrodynamic interactions may affect the formation of these shear-induced crystal phases, we stress that the non-equilibrium phase behavior for colloidal hard spheres as predicted by Brownian dynamics simulations in Ref. 16 was in good agreement with the experimental observations.

ACKNOWLEDGMENTS

This work was supported by the Netherlands Center for Multiscale Catalytic Energy Conversion (MCEC), a NWO Gravitation program funded by the Ministry of Education, Culture and Science of the government of the Netherlands. The authors gratefully thank Alfons van Blaaderen, Arnout Imhof, and Ajoy Kumar Kandar for the extensive and fruitful discussions on the subject and for encouraging this numerical investigation. G.F. thanks Ernest van der Wee and Guido Avvisati for useful discussions.

DATA AVAILABILITY

The data that support the findings of this study are available from the corresponding author upon reasonable request.

REFERENCES

- Y. A. Vlasov, N. Yao, and D. J. Norris, "Synthesis of photonic crystals for optical wavelengths from semiconductor quantum dots," *Adv. Mater.* **11**, 165–169 (1999).
- J. D. Joannopoulos, P. R. Villeneuve, and S. Fan, "Photonic crystals: Putting a new twist on light," *Nature* **386**, 143–149 (1997).
- P. D'Haene, J. Mewis, and G. G. Fuller, "Scattering dichroism measurements of flow-induced structure of a shear thickening suspension," *J. Colloid Interface Sci.* **156**, 350–358 (1993).
- J. Delhommelle, J. Petrávic, and D. J. Evans, "Non-Newtonian behavior in simple fluids," *J. Chem. Phys.* **120**, 6117–6123 (2004).
- N. Koumakis, A. B. Schofield, and G. Petekidis, "Effects of shear induced crystallization on the rheology and ageing of hard sphere glasses," *Soft Matter* **4**, 2008 (2008); [arXiv:0804.1218](https://arxiv.org/abs/0804.1218).
- Y. S. Lee and N. J. Wagner, "Dynamic properties of shear thickening colloidal suspensions," *Rheol. Acta* **42**, 199–208 (2003); [arXiv:1403.6793](https://arxiv.org/abs/1403.6793).
- J. K. G. Dhont and W. J. Briels, "Gradient and vorticity banding," *Rheol. Acta* **47**, 257–281 (2008).
- H. Löwen, "Colloidal soft matter under external control," *J. Phys.: Condens. Matter* **13**, R415–R432 (2001).
- B. Shen, J. Ricouvier, F. Malloggi, and P. Tabeling, "Designing colloidal molecules with microfluidics," *Adv. Sci.* **3**, 1600012 (2016).
- W. E. Uspsal and P. S. Doyle, "Self-organizing microfluidic crystals," *Soft Matter* **10**, 5177–5191 (2014).

- ¹¹J. Vermant and M. J. Solomon, "Flow-induced structure in colloidal suspensions," *J. Phys.: Condens. Matter* **17**, R187–R216 (2005).
- ¹²B. J. Ackerson and P. N. Pusey, "Shear induced order in suspensions of hard spheres," *Phys. Rev. Lett.* **61**, 1033–1036 (1988).
- ¹³B. J. Ackerson, "Shear induced order and shear processing of model hard sphere suspensions," *J. Rheol.* **34**, 553–590 (1990).
- ¹⁴X. Cheng, J. H. McCoy, J. N. Israelachvili, and I. Cohen, "Imaging the microscopic structure of shear thinning and thickening colloidal suspensions," *Science* **333**, 1276–1279 (2011).
- ¹⁵X. Cheng, X. Xu, S. A. Rice, A. R. Dinner, and I. Cohen, "Assembly of vorticity-aligned hard-sphere colloidal strings in a simple shear flow," *Proc. Natl. Acad. Sci. U. S. A.* **109**, 63–67 (2012).
- ¹⁶T. H. Besseling, M. Hermes, A. Fortini, M. Dijkstra, A. Imhof, and A. Van Blaaderen, "Oscillatory shear-induced 3D crystalline order in colloidal hard-sphere fluids," *Soft Matter* **8**, 6931–6939 (2012).
- ¹⁷M. D. Haw, W. C. K. Poon, and P. N. Pusey, "Direct observation of oscillatory-shear-induced order in colloidal suspensions," *Phys. Rev. E* **57**, 6859–6864 (1998).
- ¹⁸Y. D. Yan, J. K. G. Dhont, C. Smits, and H. N. W. Lekkerkerker, "Oscillatory-shear-induced order in nonaqueous dispersions of charged colloidal spheres," *Physica A* **202**, 68–80 (1994).
- ¹⁹T. Palberg and R. Biehl, "Sheared colloidal crystals in confined geometry: A real space study on stationary structures under shear," *Faraday Discuss.* **123**, 133–143 (2003).
- ²⁰R. Biehl and T. Palberg, "Modes of motion in a confined colloidal suspension under shear," *Europhys. Lett.* **66**, 291 (2004).
- ²¹A. Stipp, R. Biehl, T. Preis, J. Liu, A. B. Fontecha, H. J. Schöpe, and T. Palberg, "Heterogeneous nucleation of colloidal melts under the influence of shearing fields," *J. Phys.: Condens. Matter* **16**, S3885–S3902 (2004).
- ²²J. Ruiz-Franco, J. Marakis, N. Gnan, J. Kohlbrecher, M. Gauthier, M. Lettinga, D. Vlassopoulos, and E. Zaccarelli, "Crystal-to-crystal transition of ultrasoft colloids under shear," *Phys. Rev. Lett.* **120**, 078003 (2018).
- ²³W. Xue and G. S. Grest, "Shear-induced alignment of colloidal particles in the presence of a shear flow," *Phys. Rev. Lett.* **64**, 419–422 (1990).
- ²⁴M. J. Stevens, M. O. Robbins, and J. F. Belak, "Shear melting of colloids: A nonequilibrium phase diagram," *Phys. Rev. Lett.* **66**, 3004 (1991).
- ²⁵A. Yethiraj, A. Wouterse, B. Groh, and A. van Blaaderen, "Nature of an electric-field-induced colloidal martensitic transition," *Phys. Rev. Lett.* **92**, 058301 (2004).
- ²⁶P. S. Mohanty, P. Bagheri, S. Nöjd, A. Yethiraj, and P. Schurtenberger, "Multiple path-dependent routes for phase-transition kinetics in thermoresponsive and field-responsive ultrasoft colloids," *Phys. Rev. X* **5**, 011030 (2015).
- ²⁷Y. Peng, W. Li, F. Wang, T. Still, A. G. Yodh, and Y. Han, "Diffusive and martensitic nucleation kinetics in solid-solid transitions of colloidal crystals," *Nat. Commun.* **8**, 14978 (2017).
- ²⁸Y. Peng, F. Wang, Z. Wang, A. M. Alsayed, Z. Zhang, A. G. Yodh, and Y. Han, "Two-step nucleation mechanism in solid–solid phase transitions," *Nat. Mater.* **14**, 101–108 (2015).
- ²⁹W. Qi, Y. Peng, Y. Han, R. K. Bowles, and M. Dijkstra, "Nonclassical nucleation in a solid-solid transition of confined hard spheres," *Phys. Rev. Lett.* **115**, 185701 (2015).
- ³⁰C. X. Du, G. van Anders, R. S. Newman, and S. C. Glotzer, "Shape-driven solid–solid transitions in colloids," *Proc. Natl. Acad. Sci. U. S. A.* **114**, E3892–E3899 (2017).
- ³¹D. Wan, C. X. Du, G. van Anders, and S. C. Glotzer, "Fcc bcc phase transitions in convex and concave hard particle systems," *J. Phys. Chem. B* **123**, 9038–9043 (2019).
- ³²L. Rossi, V. Soni, D. J. Ashton, D. J. Pine, A. P. Philipse, P. M. Chaikin, M. Dijkstra, S. Sacanna, and W. T. M. Irvine, "Shape-sensitive crystallization in colloidal superball fluids," *Proc. Natl. Acad. Sci. U. S. A.* **112**, 5286–5290 (2015).
- ³³M. T. Casey, R. T. Scarlett, W. B. Rogers, I. Jenkins, T. Sinno, and J. C. Crocker, "Driving diffusionless transformations in colloidal crystals using DNA handshaking," *Nat. Commun.* **3**, 1209 (2012).
- ³⁴I. C. Jenkins, M. T. Casey, J. T. McGinley, J. C. Crocker, and T. Sinno, "Hydrodynamics selects the pathway for displacive transformations in DNA-linked colloidal crystallites," *Proc. Natl. Acad. Sci. U. S. A.* **111**, 4803–4808 (2014).
- ³⁵A. P. Hynninen and M. Dijkstra, "Phase diagrams of hard-core repulsive Yukawa particles," *Phys. Rev. E* **68**, 021407 (2003).
- ³⁶E. C. Ögüz, A. Reinmüller, H. J. Schöpe, T. Palberg, R. Messina, and H. Löwen, "Crystalline multilayers of charged colloids in soft confinement: Experiment versus theory," *J. Phys.: Condens. Matter* **24**, 464123 (2012).
- ³⁷D. L. Ermak, "A computer simulation of charged particles in solution. I. Technique and equilibrium properties," *J. Chem. Phys.* **62**, 4189–4196 (1975).
- ³⁸Y. L. Wu, D. Derks, A. van Blaaderen, and A. Imhof, "Melting and crystallization of colloidal hard-sphere suspensions under shear," *Proc. Natl. Acad. Sci. U. S. A.* **106**, 10564–10569 (2009).
- ³⁹P. J. Steinhardt, D. R. Nelson, and M. Ronchetti, "Bond-orientational order in liquids and glasses," *Phys. Rev. B* **28**, 784–805 (1983).
- ⁴⁰P.-R. Ten Wolde, M. J. Ruiz-Montero, and D. Frenkel, "Simulation of homogeneous crystal nucleation close to coexistence," *Faraday Discuss.* **104**, 93–110 (1996).
- ⁴¹W. Lechner and C. Dellago, "Accurate determination of crystal structures based on averaged local bond order parameters," *J. Chem. Phys.* **129**, 114707 (2008).
- ⁴²L. Landau and E. Lifschitz, *Quantum Mechanics* (Pergamon, 1965).
- ⁴³S. E. Paulin, B. J. Ackerson, and M. S. Wolfe, "Equilibrium and shear induced nonequilibrium phase behavior of PMMA microgel spheres," *J. Colloid Interface Sci.* **178**, 251–262 (1996).
- ⁴⁴S. Arai and H. Tanaka, "Surface-assisted single-crystal formation of charged colloids," *Nat. Phys.* **13**, 503–509 (2017).
- ⁴⁵H. Komatsugawa and S. Nosé, "Nonequilibrium molecular dynamics simulations of oscillatory sliding motion in a colloidal suspension system," *Phys. Rev. E* **51**, 5944 (1995).
- ⁴⁶J. J. Erpenbeck, "Shear viscosity of the hard-sphere fluid via nonequilibrium molecular dynamics," *Phys. Rev. Lett.* **52**, 1333 (1984).